Quantum-beat photoelectron-imaging spectroscopy of Xe in the VUV

Ruaridh Forbes
Department of Physics, University of Ottawa, 150 Louis Pasteur, Ottawa, Ontario, Canada K1N 6N5
and Department of Physics and Astronomy, University College London, Gower Street, London WC1E 6BT, England, United Kingdom

Varun Makhija*
Department of Physics, University of Ottawa, 150 Louis Pasteur, Ottawa, Ontario, Canada K1N 6N5

Jonathan G. Underwood
Department of Physics and Astronomy, University College London, Gower Street, London WC1E 6BT, England, United Kingdom

Albert Stolow
Department of Physics, University of Ottawa, 150 Louis Pasteur, Ottawa, Ontario, Canada K1N 6N5;
Department of Chemistry, University of Ottawa, 10 Marie Curie, Ottawa, Ontario, Canada K1N 6N5;
and National Research Council of Canada, 100 Sussex Drive, Ottawa, Ontario, Canada K1A 0R6

Iain Wilkinson
National Research Council of Canada, 100 Sussex Drive, Ottawa, Ontario, Canada K1A 0R6
and Methoden der Materialentwicklung, Helmholtz-Zentrum Berlin für Materialien und Energie GmbH,
Hahn-Meitner-Platz 1, 14109 Berlin, Germany

Paul Hockett† and Rune Lausten
National Research Council of Canada, 100 Sussex Drive, Ottawa, Ontario, Canada K1A 0R6

(Received 2 March 2018; published 22 June 2018)

Time-resolved pump-probe measurements of Xe, pumped at 133 nm and probed at 266 nm, are presented. The pump pulse prepared a long-lived hyperfine wave packet in the Xe $5p^5(^2P^\circ_{1/2})6s\,^2[1/2]^\circ_1$ manifold ($E = 77\,185\,\mathrm{cm}^{-1} = 9.57\,\mathrm{eV}$). The wave packet was monitored via single-photon ionization and velocity map photoelectron images were measured. The images provide angle- and time-resolved data which, when obtained over a large time window (900 ps), constitute a precision quantum-beat spectroscopy measurement of the hyperfine state splittings. Additionally, analysis of the full photoelectron image stack provides a quantum-beat imaging modality, in which the Fourier components of the photoelectron images correlated with specific beat components can be obtained. This may also permit the extraction of isotope-resolved photoelectron images in the frequency domain, in cases where nuclear spins (hence beat components) can be uniquely assigned to specific isotopes (as herein), and also provides phase information relating to the ionization dynamics. The information content of both raw and inverted image stacks is investigated, suggesting the utility of the Fourier analysis methodology in cases where images cannot be inverted.

DOI: 10.1103/PhysRevA.97.063417

I. INTRODUCTION

Quantum-beat spectroscopy (QBS) provides a time-domain route to high-resolution spectroscopic measurements [1]. In a standard scheme, a narrow wave packet (few-state superposition) is prepared, time-domain measurements are obtained, and Fourier analysis of the signal provides the high-resolution frequency-domain information sought. More generally, quantum-beat spectroscopy can be regarded as a subset of generalized wave-packet methods [2], with the specific requirement that sufficient wave-packet revivals are present in the observed temporal window to provide frequency-domain information. The applicability, and details, for a given case will therefore depend on experimental factors, e.g., time resolution and wave-packet preparation, and intrinsic systems properties, e.g., density of states and lifetimes [3,4]. Wave packets comprised of fine and hyperfine levels in rare gases and alkali-metal atoms are a notable application of QBS, since the lifetimes and level spacings are concomitant with nanosecond and picosecond experimental time scales [1,5].

In order to obtain time-domain data with good signal-to-noise ratios, an observable which responds to the wave-packet dynamics is required. In many cases, photoelectron angular distributions (PADs) provide a sufficient observable, which may be much more sensitive to underlying dynamics than photoelectron yields or energy spectra alone. In particular, the

*vmakhija@uottawa.ca
†paul@femtolab.ca

PADs are sensitive to the angular momentum couplings in the system; for the case of hyperfine interactions, this sensitivity has been investigated extensively by Berry and coworkers for sodium and lithium, prepared with nanosecond pulses [6–8]. In this pioneering atomic ionization work, PADs were measured (in a plane perpendicular to the light propagation) for different time delays and pump-probe polarization geometries, and the data obtained were sufficient to allow extraction of the photoionization matrix elements (partial-wave magnitudes and phase shifts), as well as an effective nuclear spin depolarization parameter, related to the hyperfine coupling. The analysis of the temporal evolution was hindered by both the experimental difficulty of recording PADs, rendering it feasible to record PADs at only a few pump-probe delays, and the fact that the pulse durations were non-negligible compared to the hyperfine precession (i.e., the characteristic time scale of the coherently prepared hyperfine wave packet) [7]. Nonetheless, the requisite theory and a detailed physical understanding of the hyperfine interaction were developed (see also Refs. [9,10] for related theoretical work). Subsequent work by various investigators explored this topic further, for example Bajic *et al.* [11], who investigated angle-resolved multiphoton ionization in Kr and Xe, and Reid *et al.* [12], who explored hyperfine depolarization in NO via time- and angle-resolved photoelectron measurements; in both cases, the sensitivity of PADs to hyperfine interactions was highlighted.

Xenon has two naturally occurring isotopes with nonzero nuclear spin [^{129}Xe ($I = 1/2$) and ^{131}Xe ($I = 3/2$)], and the hyperfine level structure has been well studied in the energy domain at a range of energies with a variety of methods, including fluorescence [13], saturated amplification [14] and photoionization [15–17]; for a more comprehensive overview see Ref. [18]. A range of high (energy) resolution ionization experiments incorporating the preparation of high-n Rydberg states has been performed to probe hyperfine splittings in Rydberg manifolds, including autoionizing regions, and in the cation [19,20]. Recently, photoion-photoelectron coincidence experiments provided isotopically resolved (hence I resolved) PADs from the $(^2P^\circ_{3/2})5d\,^2[3/2]^\circ_1$ state, following VUV excitation at 10.4 eV (83 876 cm^{-1}) [21]; subsequent work included detailed theoretical analysis and the first determination of the hyperfine couplings in this wavelength range [22].

In this paper, broadband femtosecond VUV pulses ($\lambda \approx 133$ nm, $E_{h\nu} \approx 9.32$ eV $= 75\,188$ cm^{-1}, $\Delta\lambda \approx 1.7$ nm, $\tau \approx 80$ fs) were used to coherently prepare hyperfine states in the Xe$(^2P^\circ_{1/2})6s\,^2[1/2]^\circ_1$ manifold [23] ($E = 77\,185$ cm$^{-1} = 9.57$ eV, NIST value [24], adapted from Ref. [15]), which were subsequently ionized with UV pulses ($\lambda = 266.45$ nm, $E_{h\nu} = 4.653$ eV $= 37\,530$ cm^{-1}, $\Delta\lambda = 3$ nm, $\tau = 50$ fs). The experimental setup and details of the VUV generation are presented in Sec. II. In the experiments, photoelectron images were obtained as a function of VUV-UV delay over a 900-ps temporal window (Sec. III A). As discussed above, temporal modulations in the PADs provide an observable sensitive to the underlying wave-packet dynamics, and these data constitute a QBS measurement. Determination of the hyperfine splittings and coupling constants from the photoelectron data is discussed in Sec. III B. The dataset additionally suggests a *quantum-beat imaging* methodology, in which beat-frequency resolved photoelectron images, and associated phase information, may be obtained: this is discussed in Sec. III C.

The raw experimental data, data processing scripts, and additional analysis notes to accompany this paper can be found online via an OSF repository [57].

II. EXPERIMENT

A. VUV-UV photoelectron imaging

The experimental setup used for the VUV-UV pump-probe photoelectron velocity-map imaging (VMI) measurements at 133 nm reported herein was almost identical to that previously reported for work using 160-nm radiation [25], and the reader is referred to that work for further details of the experimental apparatus beyond the outline sketched here. A similar VUV-UV pump-probe VMI experimental configuration has also been previously reported by Suzuki (see Ref. [26] for a summary); for further general discussion of VUV laser spectroscopies in both time and frequency domain precision spectroscopy experiments see, e.g., Ref. [27].

Briefly, the optical chain was initiated by a standard amplified titanium-sapphire laser system (Coherent Legend-Elite Duo), which provided 35-fs pulses at 795 nm at 1 kHz. A 2.5-mJ component of the total laser output, 7.5 mJ, was utilized in the experiments presented here. The beam was directed through a 70:30 beamsplitter to provide the pump and probe arms, respectively. The 1.75 mJ was frequency doubled using a 150-μm beta barium borate (β-BaB_2O_4, β-BBO), to provide 397.5-nm (2ω) pulses with an estimated pulse duration of 40 fs. The 2ω light was then separated from the fundamental by using dielectric mirrors. The 2ω pulses were then focused [Radius of curvature (ROC) = 1.5 m] into an argon-filled gas cell, where the 2ω pulse was frequency tripled by a six-wave mixing process, as described by Trabs and coworkers [28,29]. The 6ω femtosecond pulse was then separated from the driving field, and refocused, using dielectric mirrors centered at 133 nm (Layertec GmbH) at close to 0° incidence angles. The optical layout of the VUV generation chamber, and a representative spectrum of the generated radiation, is shown in Fig. 1. The spectrum was obtained with a VUV spectrometer (Resonance VS7550) in the configuration as shown in Fig. 1. The recorded spectrum is uncalibrated, but expected to be centered at $\lambda = 132.5$ nm based on the driving field wavelength, and stable as a function of driving field intensity [28,29]. Although this is somewhat to the red of the target pump transition to populate states in the $(^2P^\circ_{1/2})6s\,^2[1/2]^\circ_1$ manifold lying at $E = 77\,185$ cm^{-1} ($\lambda = 129.6$ nm), significant resonance-enhanced photoelectron signal was observed in the VMI measurements detailed below. This indicates that the wings of the pulse contained sufficient flux to drive the pump transition, and/or a slight blueshift of the spectrum from the expected central wavelength.

For photoelectron-imaging experiments, the VUV spectrometer was replaced with a VMI spectrometer [30], separated from the VUV generation chamber by a minimal thickness (0.5 mm) CaF_2 window (Crystran). For pump-probe measurements, the remaining 0.75 mJ of the fundamental transmitted through the beamsplitter was delayed using a motorized stage (Newport XML210), frequency tripled in two β-BBO crystals

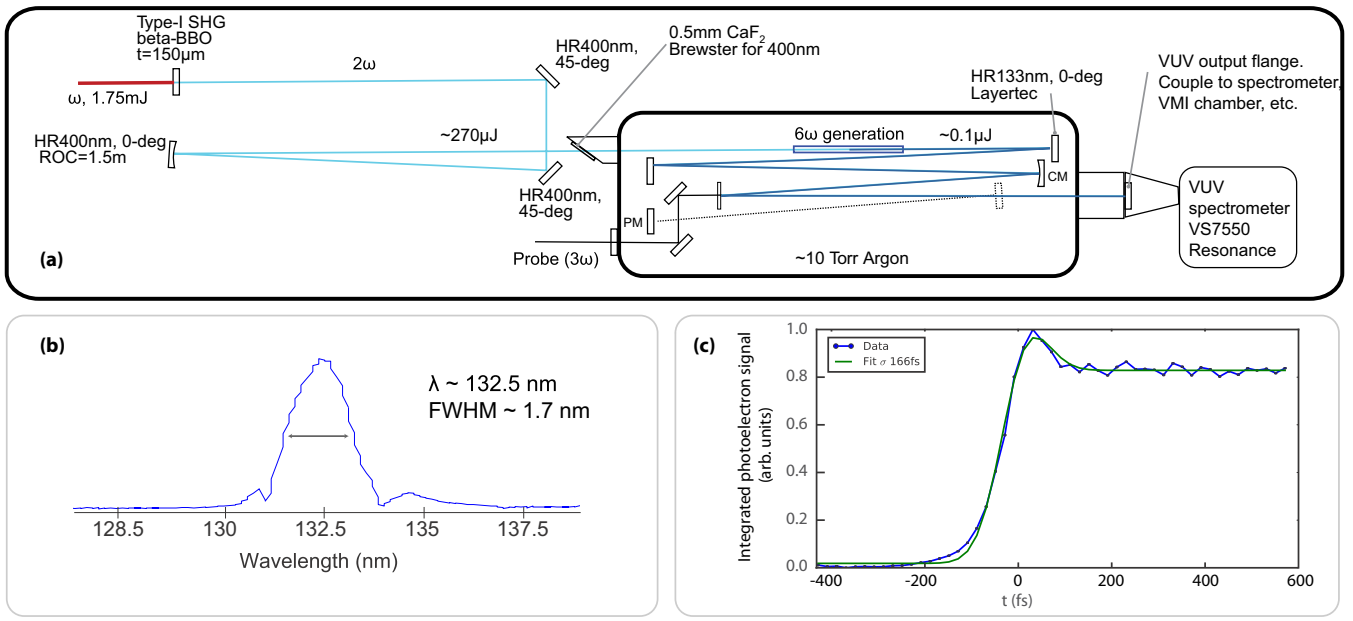

FIG. 1. (a) Layout of the 6ω generation chamber, configured to record the VUV spectrum. For photoelectron experiments, the VUV spectrometer was replaced with a VMI spectrometer. HR, high-reflector; CM, curved mirror. (b) A typical 6ω spectrum, recorded with a VUV spectrometer (Resonance VS7550, uncalibrated; see main text for details). (c) Cross-correlation measurement and fit result.

(see Ref. [25] for further details), and then recombined with the 6ω pulse, in a collinear geometry.

The pump and probe beams were focused through a set of baffles, minimizing background signals from scattered VUV and UV light, into the interaction region of a VMI spectrometer. An atomic beam of Xe was generated in a separate source chamber by expanding a 7.5% mix of Xe (Praxair Canada Inc., 5N purity) seeded in He (BOC GAZ, 5N purity) through an Even-Lavie valve [31], operating at 1 kHz and held at 40 °C, at a pressure of 20 psi (138 kPa). The supersonic expansion was skimmed, yielding an atomic beam with an estimated diameter of ∼1 mm, before entering the interaction region along the VMI time-of-flight axis. The VMI spectrometer consisted of a three-stage, open aperture repeller electrode system, and a ten-element Einzel lens stack [25]. Accelerated electrons were detected using an Micro-channel Plate (MCP)-phosphor detector setup and photoelectron images recorded by relay imaging the phosphorescence at a CCD camera (Thorlabs DC210).

Time-resolved photoelectron images were recorded for pump-probe delays between $t = -70$ and $+890$ ps in steps of 10 ps. Here, negative delay refers to the situation where the 3ω pulse arrives before the 6ω. The time-resolved photoelectron signals were constructed from the measured photoelectron images in the following manner. At each time delay of the pump and probe, two photoelectron images were recorded: one with the gas pulse temporally overlapped with the two laser pulses and one without the gas pulse (to account for ionization due to background contaminant gases and scattered light signals associated with the 6ω pulse). The "no gas" signal was then subtracted from the gas pulse data to obtain background gas and scatter free images. It is of note that no one-color photoelectron counts, barring scattered light signals, were observed with the 6ω pulse. Additionally, negligible counts with the 3ω pulse were observed with the pulse energies and MCP/phosphor voltage settings employed during the collection of the images. In total, 25 scans of the pump-probe delay window were recorded. Energy to pixel calibration was achieved by recording three-photon ionization of Xe at 266 nm under the same VMI focusing conditions utilized in the experiment.

Cross-correlation measurements made use of the same pump-probe configuration, but were obtained via scans with a higher temporal resolution (20-fs step size) over a small temporal window, as shown in Fig. 1(c). In this case three scans were sufficient, and a fit to the signal (modeled by an error function plus Gaussian line shape) provided the cross-correlation. A cross-correlation of $\tau_{xc} \approx 166$ fs [full width at half maximum (FWHM)] in the interaction region of the VMI spectrometer was determined. The non-transform-limited duration of the cross-correlation (as compared to the optimal transform-limited cross-correlation value of approximately 60 fs for these pulses) is attributed primarily to dispersion of the 6ω pulse in the CaF_2 window. In future work, a switch to an LiF window, combined with upstream dispersion compensation, should enable transform-limited 6ω pulses (approximately 40 fs) in the interaction region of the spectrometer.

B. Data processing

The energy and time-dependent photoelectron distributions can be defined in the usual way, in terms of a spherical harmonic expansion (see, e.g., Ref. [32]):

$$I(\theta,\phi,E,t) = \sum_{L,M} \beta_{L,M}(E,t) Y_{L,M}(\theta,\phi) \qquad (1)$$

where E is the photoelectron kinetic energy and t is the pump-probe delay; $\beta_{L,M}$ are the anisotropy parameters, which can be related to the photoionization dynamics of the system. For cylindrically symmetric distributions, only $M = 0$ terms are nonzero, and the ϕ coordinate is redundant: this is the

case for the measurements reported herein, and a simplified β_L notation is employed in this paper. For two-dimensional (2D) imaging of cylindrically symmetric three-dimensional (3D) distributions, in which the 3D photoelectron distribution is projected onto the detector in the measurements (sometimes termed "crush" imaging), the symmetry of the projection enables 2D slices from the original 3D photoelectron distributions to be reconstructed using standard inversion techniques [33]. To reconstruct the slices and determine the $\beta_L(E,t)$ metrics, the photoelectron images were processed using cpBasex, which implements the pBasex inversion method [34]. This method uses a fitting methodology and provides both inverted (or "slice") images, hereafter denoted by the coordinate system (x_i,y_i,t), and the associated $\beta_L(E,t)$ expansion parameters directly. For the distributions considered herein, from a two-photon process with cylindrical symmetry, the only nonzero parameters are $L = 0,2$, and 4. (For non-cylindrically-symmetric distributions, e.g., distributions arising from nonparallel pump-probe polarization geometries, direct inversion is not possible, although other methods—for instance tomographic reconstruction—can be applied with some additional experimental effort. For further general discussion on charged particle imaging and reconstruction, see Ref. [33]; for recent discussion in the context of 2D and 3D metrology techniques, including photoelectron tomography, see, for instance, Ref. [35] and references therein.)

Images were defined and processed via a variety of analysis protocols, including per-scan and scan-summed, and with and without image symmetrization. The processing of images from each experimental scan provided a way to estimate statistical uncertainties, while scan-summed and symmetrized images provided the best signal-to-noise, hence highest resolution, dataset. Other selections—e.g., summation over a subset of the scans, choice of a single quadrant from the photoelectron images, and so forth—provided additional validation and cross-checks on the extracted data. In the results reported herein, the scan-summed dataset was the main focus of the analysis, and statistical (1σ) uncertainties were determined from analysis on a per-scan basis (see also Ref. [57]).

III. RESULTS AND DISCUSSION

A. Photoelectron images

Figure 2(a) illustrates typical raw (unsymmetrized) photoelectron-imaging results at various pump-probe time delays. The images show a dramatic change in the angular dependence of the outer ring as a function of pump-probe delay, t, with clear switching from a four-lobed to two-lobed structure. At a total photon energy of 14.24 eV (114 850 cm^{-1}), there is 2.1 eV of excess energy above the first ionization threshold at 12.13 eV (97 833 cm^{-1}, values from NIST, Ref. [24], adapted from Refs. [15,36]), and two final J^+ states can be populated in the ion: (1) $\mathrm{Xe}^+(5p^5)^2P^\circ_{3/2}$ (ground state) and (2) $\mathrm{Xe}^+(5p^5)^2P^\circ_{1/2}$ (1.3 eV, 10 537 cm^{-1}). The outer photoelectron band (maximum photoelectron energy) in the images is therefore correlated with formation of the cation with $J^+ = 3/2$, while the inner ring correlates with the $J^+ = 1/2$ spin-orbit excited state; the corresponding photoelectron energies (band centers) are $E = 2.1$ and 0.8 eV, respectively.

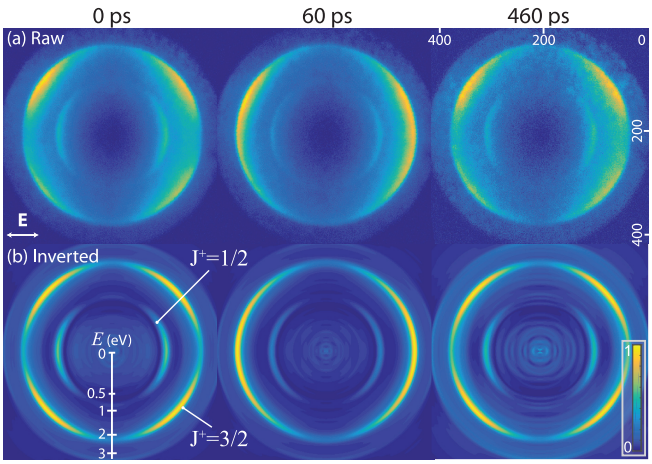

FIG. 2. Example photoelectron images. (a) Raw images, summed over experimental cycles. The electric-field polarization vectors were both horizontal, as indicated. (b) The corresponding inverted images. Photoelectron bands are labeled by the final cation states, $J^+ = \frac{1}{2}$ and $\frac{3}{2}$, corresponding to electron energies $E = 0.8$ and 2.1 eV, respectively. Scale bar shows pixel ($\propto$ velocity) to E conversion. Color maps were normalized to the maximum signal intensity for each image (arb. units). The difference between quadrants in the raw images, which should be identical by symmetry, is ascribed primarily to detector inhomogeneities, although other experimental factors may also contribute.

Inverted (slice) images are also shown in Fig. 2(b) for reference. A level diagram, showing both the excited-state levels prepared and the final ion states populated, is given in Fig. 3.

A visualization of the full (x,y,t) volume is shown in Fig. 4(a), and the inverted image volume (x_i,y_i,t) is shown in Fig. 4(b). In these renderings, only the top right quadrant of the images is included, and ten isosurfaces are shown, spaced over 10–90% photoelectron yield (normalized to the maximum volume element). The renderings give a sense of the full dataset: temporal oscillations are clearly observed, particularly in the outer photoelectron band, and some aspects of the changing angular distributions can be discerned (this is

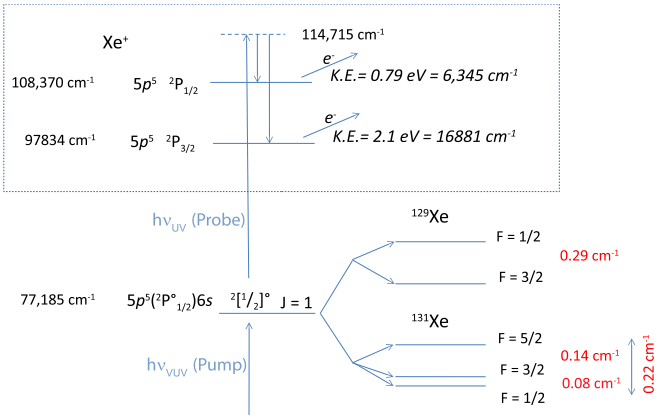

FIG. 3. Energy-level diagram for the prepared hyperfine states (lower section), and final ion states (upper section). The energies are not to scale. Values from NIST; see main text for discussion.

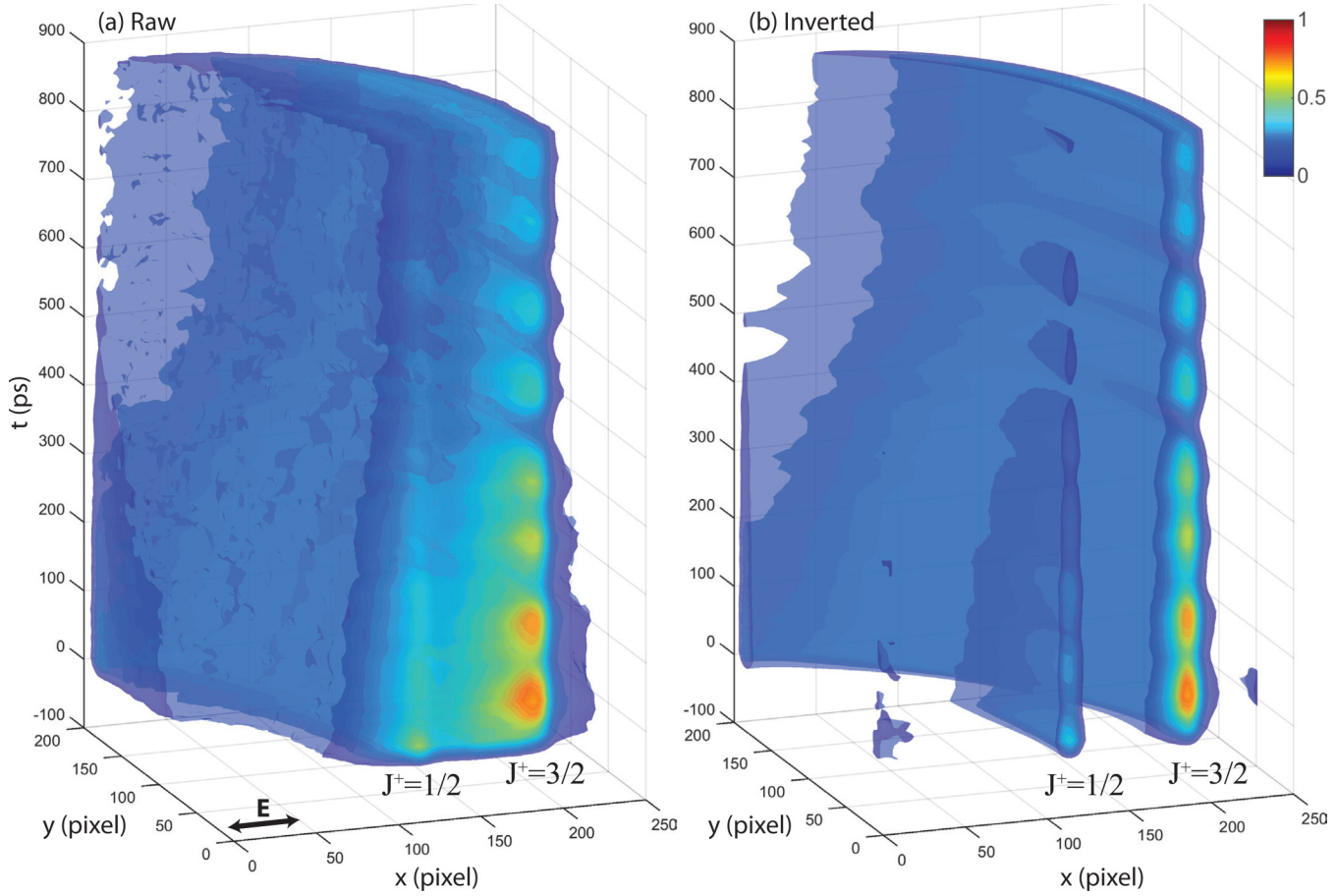

FIG. 4. Full image volumes, shown for a single quadrant. (a) Raw data (x,y,t). (b) Inverted images (x_i,y_i,t). Isosurfaces show 10–90% photoelectron signal. The full data volume was down-sampled and smoothed for these renderings.

less apparent in the static renderings, but can be seen more clearly in the interactive versions available online), although are not pronounced.

A more quantitative picture is obtained by analysis of the results in terms of the characteristic $\beta_L(\Delta E,t)$ parameters, as discussed in Sec. II B. Metrics extracted from the processed images over a small energy range ΔE, defined by the FWHM of the photoelectron features, are illustrated in Fig. 5. It is immediately apparent from these data that the PADs change significantly as a function of pump-probe delay, with clear oscillations apparent in the temporal profiles of $\beta_2(t)$ and $\beta_4(t)$ for both photoelectron bands. The oscillations are not, however, clearly observed in the photoelectron yield [denoted $\beta_0(t)$], which shows a gradual decay with only a hint of the oscillations observed in the $L > 0$ terms. This is due to the strong dependence of the PADs on the evolution of the hyperfine wave packet as a function of time, while the total yields are much less sensitive [8,12].

For the inner band ($J^+ = 1/2$), the lower photoelectron yield results in higher noise in the extracted parameters, but clear quantum beats are still observed. These beats are out of phase with the $J^+ = 3/2$ traces. Empirically, this indicates a sign change in the excited-state polarization (alignment tensor) sensitivity of the two ionizing transitions. The sign change is consistent with the treatment of Greene and Zare [9], in which a universal alignment function is derived; the sign of this function depends on angular momentum transfer, and changes between $\Delta J = 0$ and ± 1 ionizing transitions. The sign is related to the final m-state distribution, and effectively defines the degree to which the alignment is parallel (+), or perpendicular (−), relative to the E-field polarization vector. This behavior can be considered as analogous to polarization sensitivity in fluorescence measurements [1,37] although, for the photoionization case, additional terms—including the photoelectron angular momentum—play a role in determining the modulation depth (sensitivity) and the structure of the PADs [8,10].

B. Quantum-beat spectroscopy: Hyperfine structure

Figure 6 shows Fourier power spectra resulting from the Fourier transform (FT) of the $\beta_L(t)$ (Fig. 5). The corresponding feature positions and uncertainties are listed in Table I. The FTs of both $\beta_2(t)$ and $\beta_4(t)$ provide the frequency domain parameters $\beta_2(\nu)$ and $\beta_4(\nu)$ associated with both spin-orbit states of the cation. The major features are located around 0.14 and 0.29 cm^{-1}, and minor features around 0.09 and 0.22 cm^{-1} are observed in some channels. The FTs of the photoelectron yields $[\beta_0(\nu)]$ reveal very little frequency structure, apart from the lowest frequency feature.

The frequencies listed in Table I correspond to the peak positions of the frequencies observed in the FTs from the major

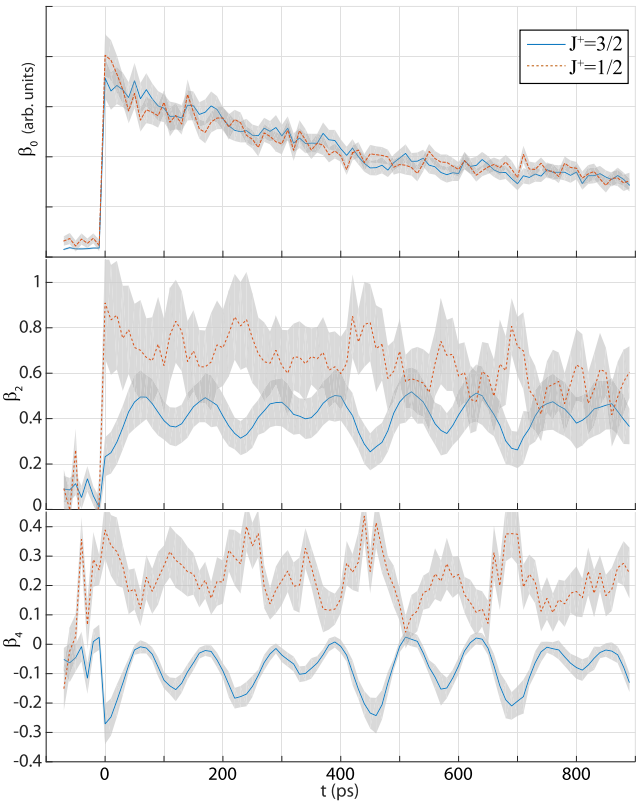

FIG. 5. Time-dependent $\beta_L(t)$ parameters, $J^+ = 3/2$ (blue, solid) and 1/2 (orange, dashed). Uncertainties show statistical errors (1σ), determined from analysis of each experimental cycle; see Sec. II B for details.

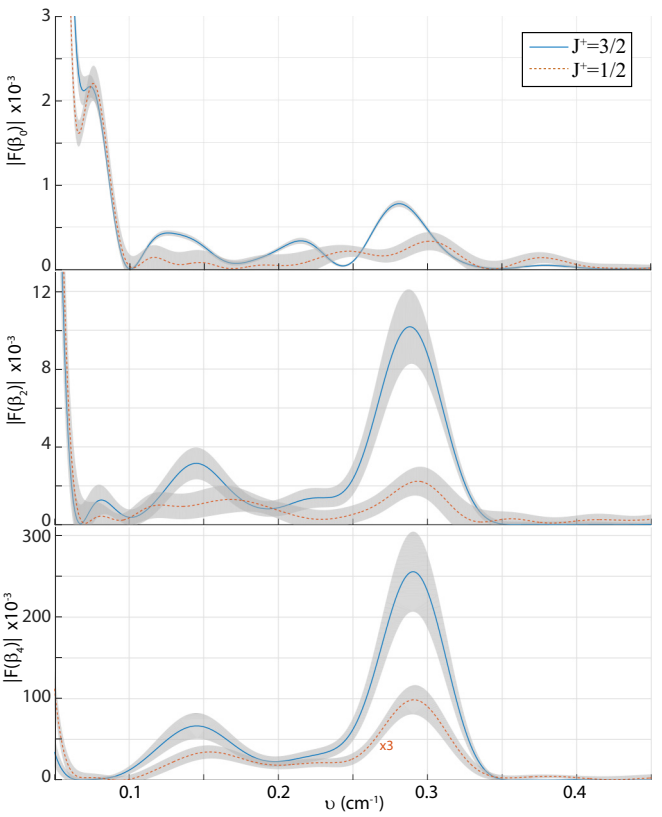

FIG. 6. Frequency domain results $\beta_L(\upsilon)$, obtained via Fourier transform of the $\beta_L(t)$ data shown in Fig. 5. Plots show the Fourier power spectrum for each trace, with statistical uncertainties (1σ), determined from analysis of each experimental cycle; see Sec. II B for details.

($J^+ = 3/2$) feature [38], and are reported with uncertainties determined from propagation of the 1σ errors, extracted by analysis of each scan, as detailed in Sec. II B. The statistical uncertainties determined in this manner, on the order of 10^{-3} cm^{-1}, are an order of magnitude better than the absolute frequency limits imposed by the 890-ps temporal window. This corresponds to a lower limit on the observable frequency of $\nu_{\min} = 3.75 \times 10^{-2}$ cm^{-1}, and defines the resolution of the FT; this limit is also reflected in the feature widths, which are on the same order as $\nu_{\min}$. The statistical uncertainties are, however, significantly poorer than the absolute experimental frequency accuracy, which is defined by the timing uncertainty of the measurements: in this case, the pump-probe cross-correlation of the laser pulses, $\tau_{xc} \approx 170$ fs (dispersion limited in the current experiments), which defines a frequency accuracy $\nu_{xc} = 6.2 \times 10^{-6}$ cm^{-1}. The upper limit on the observable frequency is defined by the temporal sampling step size, $\tau_s = 10$ ps, which results in $\nu_{\max} = 3.335$ cm^{-1}.

From the measurements, the hyperfine coupling constants can be determined by fitting to the usual form (see, e.g., Ref. [18]):

$$\Delta E_{(F,F-1)} = AF + \frac{3}{2}BF\left(\frac{F^2 + \frac{1}{2} - J(J+1) - I(I+1)}{IJ(2J-1)(2I-1)}\right), \tag{2}$$

where A is the magnetic dipole constant, and B is the electric quadrupole constant. Hyperfine constants determined in this manner are reported in Table I, and compared with previously reported values. In one case—A for ^{131}Xe—the constant is

TABLE I. Measured level splittings and the hyperfine constants determined. Statistical uncertainty estimates are given for the measurements. Literature values are reproduced from Ref. [18], Table II, with D'Amico *et al.* [18], Jackson and Coulombe [43], and Fischer *et al.* [44].

			Hyperfine constants		Literature	
Isotope	F, F'	Splitting (cm^{-1})	A (MHz)	B (MHz)	A (MHz)	B (MHz)
129 ($I = 1/2$)	1/2, 3/2	0.2863 (5)	−5723 (9)		−5808 (2) [18], −5806 (4) [43], −5799 (9) [44]	
131 ($I = 3/2$)	3/2, 1/2	0.0855 (10)	1697 (30)	−8 (7)	1709.3 (7) [18], 1710 (6) [43], 1716 (3) [44]	30.3 (8) [18],
	5/2, 3/2	0.1411 (29)				16 (3) [43], 24 (6) [44]
	5/2, 1/2	0.2276 (29)				

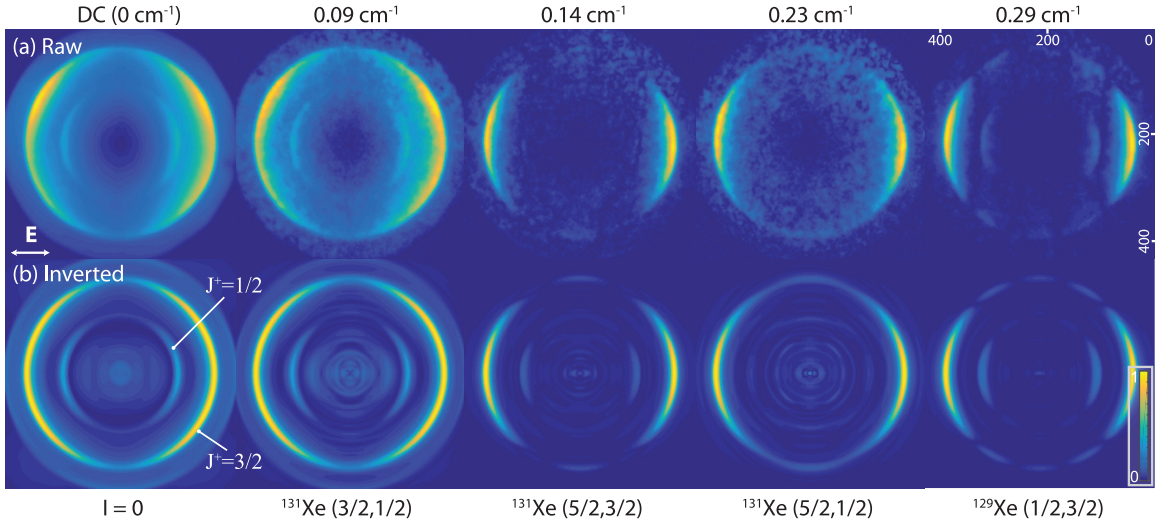

FIG. 7. Fourier image components (absolute value) corresponding to the observed features (see Fig. 6 and Table I). (a) FT images from the raw image stack. (b) FT images from the inverted image stack. Full image stacks are shown in Fig. 8. Color maps were normalized independently for each image.

comparable to those previously determined within the experimental uncertainty; in the remaining cases, the constants are comparable to those previously determined, but not within the experimental uncertainties. This may indicate systematic errors in the experiment and/or data analysis; the presence of electric fields (on the order of 10–50 V cm^{-1} in the present case) in the VMI spectrometer is potentially one source of small shifts (sub-cm^{-1}) on the measured splittings, particularly since the Stark shifts are I and F dependent [39], and a relatively high-lying manifold is accessed. Detailed exploration of this effect remains for future work, although rough estimates on the scale of the effect for Rydberg states can be made from a hydrogenic model [40,41]. In this model, Stark splitting between adjacent levels is given by $\Delta E_s = 1.28 \times 10^{-4} n\varepsilon$, where ε is the field strength in V cm^{-1}. This indicates $\Delta E_s = 0.04$ cm^{-1} for $n = 6$ and $\varepsilon = 50$ V cm^{-1}, which is significant on the scale of the measured splittings. However, it is of note that previous high-resolution studies of higher n manifolds ($n > 10$), at higher field strengths of $\varepsilon \sim 100$ V cm^{-1}, have neglected such effects [42]. The polarizabilities of the relevant states in Xe required to calculate ΔE_s accurately [39] are, to the best of our knowledge, not known.

C. Quantum-beat imaging

1. Phenomenology

For a quantum-beat imaging methodology, the full (x,y,t) data volume can be transformed directly to the frequency domain via application of an FT to each pixel. This is a different approach from the treatment of the $\beta_L(t)$ parameters detailed above, since it does not require inversion of the raw image stack. Hence, it is directly applicable even for the case of complex, noninvertable images (see Sec. II B). The resulting (x,y,ν) images provide the Fourier components of the time-resolved photoelectron images [45]. In cases where inversion is applicable, the processed data volume (x_i,y_i,t) can be similarly transformed.

In the present case, the frequency components correspond to the hyperfine level splittings, and there is separation of the $I = 0$ isotopes from the $I \neq 0$ isotopes in the frequency domain, since only the latter can contribute to the time dependence of the signal (i.e., $\nu > 0$), while the former will only contribute to the time-independent (dc) part of the signal (i.e., $\nu = 0$). Furthermore, if the Fourier components are uniquely associated with a particular isotope, then different frequency-domain images will correspond to isotopically resolved wave-packet components and associated frequency-domain photoelectron images. For this assertion to be valid, the isotope signals must be incoherent, and the level splittings must be resolved in the frequency domain. If these conditions hold, then the Fourier components provide a means to obtain isotopically resolved photoelectron distributions, each correlated with pairs of hyperfine states. (This is conceptually similar to the recent photoelectron-photoion coincidence measurements mentioned previously [21,22], except that the information obtained is a set of Fourier image components from a dynamical system, rather than state resolved photoelectron distributions.)

Figures 7 and 8 illustrate the Fourier domain images (absolute values). The main discrete frequency components, correlated with the level splittings given in Table I, are shown in Fig. 7; Fig. 8 provides renderings of the full frequency domain image volumes. A number of phenomenological observations may be made from these results.

In both sets of images, the angular features are peaked along the laser polarization axis (x axis, corresponding to positive β_2), and this appears to be the dominant contribution in all cases. In terms of the hyperfine wave packet, the images correlate with beat frequencies, hence pairs of F levels. The photoelectron interference pattern for each pair therefore contains two contributions [8]: (1) the "intrinsic" photoionization interferences, due to the partial-wave composition of the continuum wave function, which would be observed for ionization of a single (eigen)state; and (2) additional interferences which arise in the sum over pairs of F states, and include a time

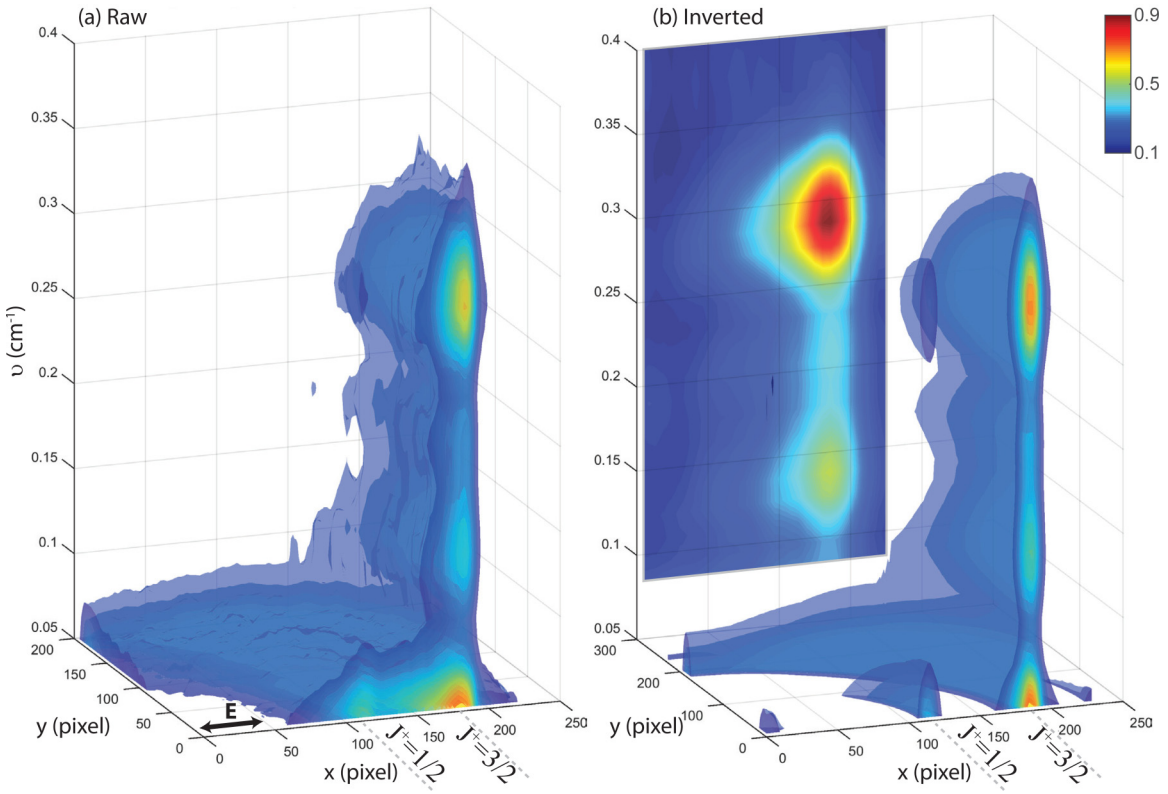

FIG. 8. Fourier image volumes (absolute values, single quadrant). (a) FT of the raw image stack (x,y,ν). (b) FT of the inverted image stack (x_i,y_i,ν); back-panel inset shows a detailed view of the (x_i,ν) plane in the region of the $J^+ = 3/2$ features (x_i = 165–200 pixels). Isosurfaces show 10–90% photoelectron signal. The full data volume was down-sampled and smoothed for these renderings. The main features correspond to the images shown in Fig. 7.

dependence due to the time evolution of the prepared wave packet.

In the case of ^{131}Xe, there is an additional layer of complexity, since there are multiple F pairs which contribute to the final photoelectron images. In these results, it appears that interference between the components [46] at 0.09 and 0.14 cm^{-1}—which have lobes with different angular spreads (see Fig. 7)—is the main source of the $\beta_4(t)$ oscillations observed (Figs. 5 and 6); this is also consistent with the lack of a $\beta_4(\nu)$ feature at 0.09 cm^{-1} (Fig. 6). In contrast, for ^{129}Xe only a single Fourier image component is present (0.29 cm^{-1}), indicating that any $\beta_4(t)$ oscillations correlated with this isotope originate from just this F pair; this is consistent with the significant $\beta_4(\nu)$ feature observed at this frequency (Fig. 6). This is also suggested by the greater angular complexity in the images (higher L terms), as compared to the ^{131}Xe images. This is observed most clearly in the inverted image, which contains multiple lobes for both spectral features. The images in this case therefore indicate that the intrinsic ionization dynamics of the two F states involved would result in different fourfold distributions. However, quantitative analysis along these lines requires knowledge of the photoionization matrix elements, either from calculation or via retrieval from experimental data. In the latter case, previous work has shown that this may be possible for hyperfine wave-packet data [6–8], and the data obtained in this work may also contain sufficient information for such a retrieval. Work is ongoing in this direction, and some general comments are presented in the following section.

Another interesting feature of the images presented in Fig. 7 is the absence of any appreciable intensity in the inner ring for the images correlated with 0.14 and 0.23 cm^{-1}. This indicates that the associated components of the hyperfine wave packet were inefficiently probed, with little ionization to the $J^+ = 1/2$ state of the cation. Finally, it is interesting to note that the widths (radial spread) of the features are not constant. This is seen most clearly in the inverted image volumes of Fig. 8(b), but is also apparent in the inverted images of Fig. 7. In particular, the 0.29-cm^{-1} feature has a larger radial extent that the 0.14-cm^{-1} feature, indicating slight changes in the photoelectron energy spectra associated with these components.

2. *Phase imaging and wave-packet treatment*

In the preceding discussion, the quantum-beat imaging results were presented along with a basic phenomenological discussion. Further insight into the results can be obtained via the associated phase structure of the (x,y,ν) data. Figure 9 shows the phase images for the observed features, for both the raw and inverted images, corresponding to the absolute value images shown in Fig. 7. Broadly speaking, the phase structures are similar for both the raw and inverted images, indicating the possibility of accessing phase information directly from the raw image stacks as suggested previously. Unsurprisingly, the inverted images contain a clearer and more pronounced phase structure [47]. This occurs simply because the photoelectron features do not overlap in the inverted (slice)

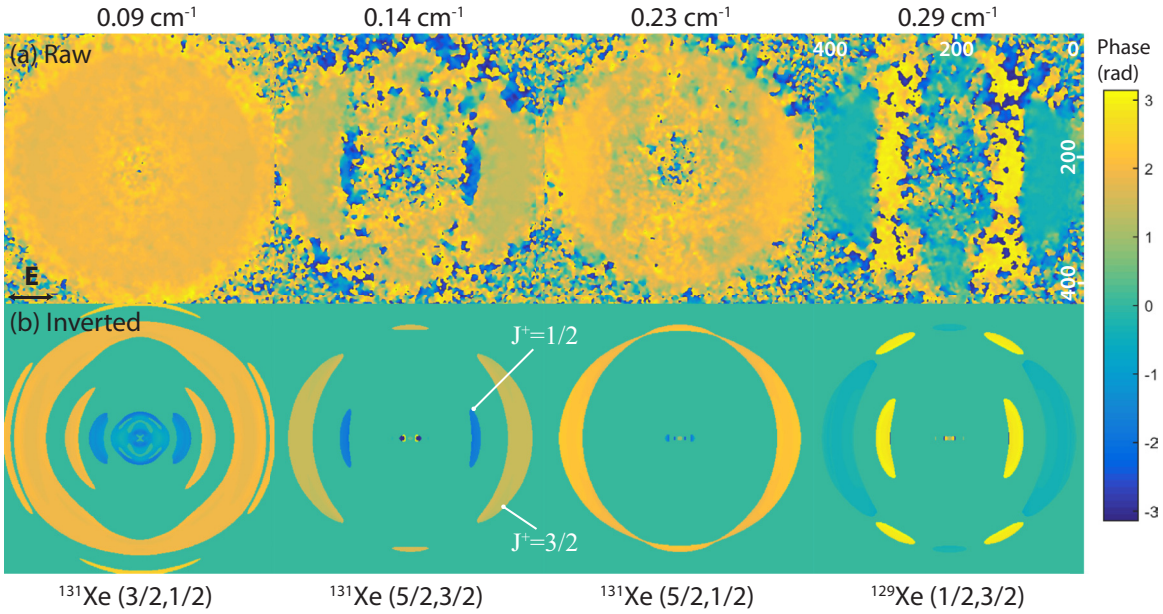

FIG. 9. Fourier image components (phases) corresponding to the observed features (see Fig. 6 and Table I). (a) FT images from the raw image stack. (b) FT images from the inverted image stack. The corresponding absolute value images are presented in Fig. 7.

images, which show clear rings and associated phases; in contrast, the raw (crush) images show continuous spatial phase structure.

Exploration of the phase structure in the images provides an alternative analysis methodology which can be compared with many of the observations previously discussed. For instance, the inner and outer photoelectron bands are out of phase; this effect is particularly clear in the 0.14- and 0.29-cm^{-1} features, and is in agreement with the phase shift observed in the $\beta_L(t)$ plots pertaining to the two different final states (Fig. 5). The appearance of additional angular structure in the 0.29-cm^{-1} feature, discussed in the previous section as a result of different final continuum states related to each ionizing F state, is now made clearer by the alternating phase pattern in the outer ring. This phase structure indicates the phase difference between the two F state contributions, with the equatorial region shifted from the fourfold lobe structure by just over π radians. This phase structure quantitatively maps the change in angular structure as a function of t observed in the original time-domain images (Fig. 2).

A formal statement of the phase contributions can be obtained from a wave-packet treatment, in which the full complexity of the photoionization dynamics remains implicit. In general, the signal for a PAD measured by one-photon ionization with linearly polarized light from a wave packet can be written as

$$I(\theta,E,t) \propto |\langle \Psi(t)|\mu_Z|\Phi_f^+\psi_e(E,\theta)\rangle|^2. \tag{3}$$

Here $\Psi(t)$ is the bound wave packet, μ_Z is the dipole moment along the polarization direction of the light, and Φ_f^+ and $\psi_e(E,\theta)$ are the final ionic state and photoelectron wave functions, respectively. To begin with, assume that the wave packet is a superposition of two hyperfine components:

$$\Psi(t) = c_1 e^{iE_1/\hbar t}|F_1\rangle + c_2 e^{iE_2/\hbar t}|F_2\rangle \tag{4}$$

where c_i and E_i are the coefficients and energies of the hyperfine states. Inserting this into Eq. (3) and expanding gives

$$I(\theta,E,t) = P_1\left|d_1^f\right|^2 + P_2\left|d_2^f\right|^2 + c_1^* c_2 d_1^f d_2^{f*} e^{i\Omega t} + c_1 c_2^* d_1^{f*} d_2^f e^{-i\Omega t}. \tag{5}$$

$P_1 = |c_1|^2$ and $P_2 = |c_2|^2$ are the populations of the two hyperfine states. $d_1^f = \langle F_1|\mu_Z|\Phi_f^+\psi_e(E,\theta)\rangle$ is the ionization dipole matrix out of the F_1 state, and d_2^f is the same out of F_2. The dependence of these on E and θ is implicit. $\Omega = (E_2 - E1)/\hbar$ is the angular beat frequency between the hyperfine states. Note that the last two terms in the above expression are conjugates. As a result, if the dipole matrix elements and wave-packet coefficients are expressed in terms of their amplitudes and phases, the following expression results:

$$I(\theta,E,t) = P_1\left|d_1^f\right|^2 + P_2\left|d_2^f\right|^2 + 2|c_1||c_2|\left|d_1^f\right|\left|d_2^f\right| \times \cos\left[\Omega t + \Delta\phi_{1,2}^c + \Delta\phi_{1,2}^f\right]. \tag{6}$$

From this expression the images obtained by the FT of $I(\theta,E,t)$ can be understood.

The $I(\theta,E,\nu=0)$ image corresponding to the dc component of the FT is given by $P_1|d_1^f|^2 + P_2|d_2^f|^2$. The angle and energy dependent structure in these images is therefore entirely determined by the magnitudes of the ionization dipoles out of each component state. The contribution of each component state is determined by their populations. These images will have only a real component, and reflect the "intrinsic" photoionization dynamics, hence the sum over the corresponding PADs from each component state.

The $I(\theta,E,\nu)$ images corresponding to the beat frequencies on the other hand should have an amplitude and phase. The structure in the amplitude image is determined by the product of the ionization dipoles—$|d_1^f(E,\theta)||d_2^f(E,\theta)|$—and that of the phase image is determined by the phase difference

between the ionization dipoles—$\Delta\phi^{f}_{1,2}(E,\theta)$. Note that both the amplitude and phase are offset by constants determined by the product of the magnitudes of the wave-packet coefficients and their phase differences ($\Delta\phi^{c}_{1,2}$), respectively. As such these images represent a direct measurement of the interfering ionization pathways out of the component states of the wave packet. Equation (6) can be easily generalized to a wave packet of N component eigenstates:

$$I(\theta,E,t) = \sum_{i} P_i \left|d_i^f\right|^2 + \sum_{j<k} 2|c_j||c_k|\left|d_j^f\right|\left|d_k^f\right| \times \cos\left[\Omega t + \Delta\phi^{c}_{j,k} + \Delta\phi^{f}_{j,k}\right]. \quad (7)$$

The indices i, j, and k run over all N states. Thus in the case where numerous eigenstates compose the wave packet, the FT images for each beat frequency correspond to interference patterns resulting from ionization of each pair of states.

IV. CONCLUSIONS AND FUTURE WORK

In this paper, the combination of a femtosecond 130-nm VUV source with a pump-probe methodology and photoelectron-imaging measurements has been demonstrated, and used to probe a hyperfine wave packet in Xe. The measurement of images over a large time window, with high timing accuracy, provided hyperfine splittings and coupling constants which were compared with literature values. The full imaging data were also investigated in the frequency domain, and the retrieval of images correlated with different isotopes and wave-packet components, via FT of the image volume, was demonstrated and explored.

From a QBS perspective, the use of a femtosecond VUV source (ideally tuneable), combined with a UV ionization probe, provides a method applicable to a range of systems, and which can be used to interrogate high-lying manifolds which are typically hard to access [16,20]. Broadband laser pulses are also suitable for cases with larger level splittings, hence QBS of lighter elements. For an extended discussion of recent developments in precision laser spectroscopies in the VUV and XUV, see Ref. [27]. For short pulses, limitations on frequency resolution are placed, effectively, only by the temporal sampling parameters of the measurements. The difficulty of such measurements lies, instead, in the lengthy experimental runs that may be required for very high-precision measurements, and consequent requirements for long-term experimental stability. The ability to extract frequency-correlated images is an interesting property of time-resolved photoelectron-imaging experiments with sufficient spatiotemporal sampling (data volume), and allows for beat-component and isotope-correlated imaging in favorable cases, as demonstrated herein.

From a more general time-domain spectroscopy perspective, the results presented herein are a subset of wave-packet measurements. In this vein, there is a significant literature on time-resolved photoelectron spectroscopy and imaging, PADs, and related work (see, for instance, Ref. [48] for a basic introduction and Refs. [49–55] for further discussion and review). Despite this extant work, a Fourier transform photoelectron-imaging methodology has not previously been explored, to the best of our knowledge. Since the analysis methodology is somewhat obvious, in the sense that it is a clear extension of standard (but lower dimensionality) time-domain analyses, this is presumably due to the lack of sufficient data volumes in other cases. Many factors may contribute here, including the native time scale and complexity of the process under study, the experimental difficulty of obtaining sufficient measurements, or additional sampling constraints. Despite these challenges, the ability to obtain some phase information directly from the raw images is, potentially, an interesting feature of this type of analysis and may motivate future studies.

Apart from the image processing and determination of the hyperfine coupling constants, the analysis presented herein is relatively phenomenological. As mentioned above, future work will aim to address this point by consideration of both the hyperfine wave-packet and photoionization dynamics in more detail, making use of the formalism developed by Berry and coworkers [8]. Such investigation is, necessarily, rather involved, but would provide a more detailed insight into the import of the FT images presented herein, and the information content of the quantum-beat imaging methodology. In the case of a sufficiently high information content, it is possible that the full photoionization dynamics and wave-packet dynamics could be retrieved/reconstructed from the experimental data—this would be a form of "complete" experiment in photoionization terminology, and can also be considered as a form of quantum metrology [54–56].

Raw data, processing routines, and additional analysis documentation are available via an online OSF repository [57]. This repository provides a complete reporting of the analysis routines (MATLAB scripts), including full details of the image processing and Fourier transform routines (which included zero-padding and a Hann window function in the results shown herein), for readers who wish to explore the technique in further detail or build on the code-base developed.

ACKNOWLEDGMENTS

We are grateful to Andrey Boguslavskiy, Denis Guay, and Doug Moffat for assistance with the experimental infrastructure, and technical support. A.S. thanks the Natural Sciences and Engineering Research Council of Canada Discovery Grant program for financial support.

[1] S. Haroche, J. A. Paisner, and A. L. Schawlow, Phys. Rev. Lett. **30**, 948 (1973).

[2] D. J. Tannor, *Introduction to Quantum Mechanics: A Time-Dependent Perspective* (University Science Books, California, 2007).

[3] E. Hack and J. R. Huber, Int. Rev. Phys. Chem. **10**, 287 (1991).

[4] K. Blum, *Density Matrix Theory and Applications* (Springer, New York, 1996).

[5] E. Arimondo, M. Inguscio, and P. Violino, Rev. Mod. Phys. **49**, 31 (1977).

[6] M. P. Strand, J. Hansen, R.-L. Chien, and R. Berry, Chem. Phys. Lett. **59**, 205 (1978).

[7] J. C. Hansen, J. A. Duncanson, R.-L. Chien, and R. S. Berry, Phys. Rev. A **21**, 222 (1980).

[8] R.-l. Chien, O. C. Mullins, and R. S. Berry, Phys. Rev. A **28**, 2078 (1983).

[9] C. H. Greene and R. N. Zare, Phys. Rev. A **25**, 2031 (1982).

[10] H. Klar and H. Kleinpoppen, J. Phys. B **15**, 933 (1982).

[11] S. J. Bajic, R. N. Compton, X. Tang, and P. Lambropoulos, Phys. Rev. A **44**, 2102 (1991).

[12] K. L. Reid, S. P. Duxon, and M. Towrie, Chem. Phys. Lett. **228**, 351 (1994).

[13] T. Meier, H. Hühnermann, and H. Wagner, Opt. Commun. **20**, 397 (1977).

[14] P. Cahuzac and R. Vetter, Phys. Rev. Lett. **34**, 1070 (1975).

[15] F. Brandi, I. Velchev, W. Hogervorst, and W. Ubachs, Phys. Rev. A **64**, 032505 (2001).

[16] T. A. Paul and F. Merkt, J. Phys. B **38**, 4145 (2005).

[17] H. J. Wörner, M. Grütter, E. Vliegen, and F. Merkt, Phys. Rev. A **71**, 052504 (2005).

[18] G. D'Amico, G. Pesce, and A. Sasso, Phys. Rev. A **60**, 4409 (1999).

[19] M. Schäfer, M. Raunhardt, and F. Merkt, Phys. Rev. A **81**, 032514 (2010).

[20] V. L. Sukhorukov, I. D. Petrov, M. Schäfer, F. Merkt, M.-W. Ruf, and H. Hotop, J. Phys. B **45**, 092001 (2012).

[21] P. O'Keeffe, E. V. Gryzlova, D. Cubaynes, G. A. Garcia, L. Nahon, A. N. Grum-Grzhimailo, and M. Meyer, Phys. Rev. Lett. **111**, 243002 (2013).

[22] E. V. Gryzlova, P. O'Keeffe, D. Cubaynes, G. A. Garcia, L. Nahon, A. N. Grum-Grzhimailo, and M. Meyer, New J. Phys. **17**, 043054 (2015).

[23] In Racah notation, where the core is given by the term symbol $(^{2S+1}L_J)$ and the excited electron is defined by $nl^{2S+1}[K]_{J_e}$, where $K = J + l$ and $J_e = K + s$.

[24] A. Kramida, Y. Ralchenko, J. Reader, and N. A. Team, NIST Atomic Spectra Database, Version 5.5.2, 2018, https://physics.nist.gov/asd.

[25] R. Forbes, V. Makhija, K. Veyrinas, A. Stolow, J. W. L. Lee, M. Burt, M. Brouard, C. Vallance, I. Wilkinson, R. Lausten, and P. Hockett, J. Chem. Phys. **147**, 013911 (2017).

[26] T. Suzuki, J. Phys. B **47**, 124001 (2014).

[27] K. S. Eikema and W. Ubachs, in *Handbook of High-resolution Spectroscopy* (Wiley, New York, 2011).

[28] P. Trabs, Generation and utilization of femtosecond light pulses in the vacuum-ultraviolet spectral regime, Ph.D. thesis, Freien Universität Berlin, 2015, accessed on 22 Feb. 2018, https://refubium.fu-berlin.de/handle/fub188/8332.

[29] P. Trabs, H.-H. Ritze, and F. Noack, in *Proceedings of the OSA Conference on Lasers and Electro-Optics*, OSA Technical Digest (online) (Optical Society of America, 2016), paper FM4A.4.

[30] A. T. J. B. Eppink and D. H. Parker, Rev. Sci. Instrum. **68**, 3477 (1997).

[31] U. Even, J. Jortner, D. Noy, N. Lavie, and C. Cossart-Magos, J. Chem. Phys. **112**, 8068 (2000).

[32] K. L. Reid, Annu. Rev. Phys. Chem. **54**, 397 (2003).

[33] *Imaging in Molecular Dynamics*, edited by B. J. Whitaker (Cambridge University, Cambridge, England, 2003).

[34] G. A. Garcia, L. Nahon, and I. Powis, Rev. Sci. Instrum. **75**, 4989 (2004).

[35] P. Hockett, C. Lux, M. Wollenhaupt, and T. Baumert, Phys. Rev. A **92**, 013412 (2015).

[36] R. D. Knight and L.-G. Wang, J. Opt. Soc. Am. B **2**, 1084 (1985).

[37] U. Fano and J. H. Macek, Rev. Mod. Phys. **45**, 553 (1973).

[38] Slight shifts in the features for the minor channel ($J^+ = 1/2$) were observed in some cases, and the statistical uncertainties were significantly larger. Both effects were attributed to the worse signal-to-noise ratio for the minor feature (see Fig. 5).

[39] J. R. P. Angel and P. G. H. Sandars, Proc. R. Soc. A **305**, 125 (1968).

[40] M. L. Zimmerman, M. G. Littman, M. M. Kash, and D. Kleppner, Phys. Rev. A **20**, 2251 (1979).

[41] W. A. Chupka, J. Chem. Phys. **98**, 4520 (1993).

[42] M. Kono, Y. He, K. G. H. Baldwin, and B. J. Orr, J. Phys. B **46**, 035401 (2013).

[43] D. A. Jackson and M. C. Coulombe, Proc. R. Soc. A **327**, 137 (1972).

[44] W. Fischer, H. Hühnermann, G. Krömer, and H. J. Schäfer, Z. Phys. **270**, 113 (1974).

[45] By analogy with other imaging techniques, this can also be termed "hyperspectral."

[46] More precisely, between the underlying photoelectron wave functions correlated with each of the three F states involved.

[47] It is of note here that the inverted phase images include an intensity mask, with a threshold at ≈5% of the photoelectron yield, to remove spurious phase noise in energy regions with no signal.

[48] G. Wu, P. Hockett, and A. Stolow, Phys. Chem. Chem. Phys. **13**, 18447 (2011).

[49] T. Suzuki and B. J. Whitaker, Int. Rev. Phys. Chem. **20**, 313 (2001).

[50] T. Seideman, Phys. Rev. A **64**, 042504 (2001).

[51] T. Suzuki, Annu. Rev. Phys. Chem. **57**, 555 (2006).

[52] A. Stolow and J. G. Underwood, in *Advances in Chemical Physics* (Wiley, New York, 2008), pp. 497–584.

[53] K. L. Reid, Mol. Phys. **110**, 131 (2012).

[54] P. Hockett, *Quantum Metrology with Photoelectrons, Volume 1: Foundations* (Morgan & Claypool, for IOP Concise Physics, San Rafael, CA, 2018).

[55] P. Hockett, *Quantum Metrology with Photoelectrons, Volume 2: Applications and Advances* (Morgan & Claypool, for IOP Concise Physics, San Rafael, CA, 2018).

[56] H. Kleinpoppen, B. Lohmann, and A. N. Grum-Grzhimailo, *Perfect/Complete Scattering Experiments* (Springer, Berlin, 2013).

[57] Quantum Beat Photoelectron Imaging Spectroscopy of Xe in the VUV, http://dx.doi.org/10.17605/OSF.IO/DS8MK.